Nonstationary Shape Activities: Dynamic Models for Landmark Shape Change and Applications

Samarjit Das, *Student Member, IEEE,* and Namrata Vaswani, *Member, IEEE,*

Abstract—The goal of this work is to develop statistical models for the shape change of a configuration of "landmark" points (key points of interest) over time and to use these models for filtering, tracking to automatically extract landmarks, synthesis and change detection. The term "shape activity" was introduced in recent work to denote a particular stochastic model for the dynamics of landmark shapes (dynamics after global translation, scale and rotation effects are normalized for). In that work, only models for stationary shape sequences were proposed. But most "activities" of a set of landmarks, e.g. running, jumping or crawling have large shape changes w.r.t initial shape and hence nonstationary. The key contribution of this work is a novel approach to define a generative model for both 2D and 3D nonstationary landmark shape sequences. We demonstrate the use of our nonstationary model for (a) sequentially filtering noise-corrupted landmark configurations to compute Minimum Mean Procrustes Square Error (MMPSE) estimates of the true shape; (b) for tracking, i.e. for using the filtering to predict the locations of the landmarks at the current time and using this prediction for faster and more accurate landmarks extraction from the current image; (c) for synthesis and (d) for change detection. Greatly improved performance over existing work is demonstrated for filtering and for tracking landmarks from human activity videos such as those of running or jumping.

Index Terms—Landmark shape sequence analysis, nonstationary shape sequences, Kendall's shape space, tangent space, tracking, particle filtering

1 Introduction

The goal of this work is to develop statistical models for the shape change of a configuration of "landmark" points (key points of interest) over time and to use these models for filtering, tracking (to automatically extract landmarks), synthesis and change detection applications. We mainly focus on the first two applications while demonstrating promising preliminary results for the last two. "Shape" of an ordered set of landmarks was defined by Kendall [3] as all the geometric information that remains when location, scale and rotational effects are filtered out. The term "shape activity" was introduced in [4] to denote a particular stochastic model for the dynamics of "landmark shapes" (dynamics after global translation, scale and rotation effects are normalized for). A model for shape change is invariant to camera motion under the weak perspective model (also referred to as the scaled orthographic camera) [5] which is a valid assumption when the scene depth is small compared to distance from the camera. The models studied in [4] were primarily for modeling stationary shape activities (SSA) of 2D landmarks (assume constant "mean shape"). In this work we propose models for the dynamics of nonstationary shape sequences (referred to as "nonstationary shape activities" (NSSA)) of 2D and of 3D landmarks. Most "activities" of a set of landmarks, for e.g. see Fig. 8, are not stationary and hence this more general model is needed. Even if the activity is actually stationary it still gets tracked using our model.

2D landmarks are usually the 2D coordinates of feature points of interest in an image sequence, for example these could be the joints of the different body parts of the human body and the goal could be to model and track articulated human body motion (see Fig. 8, 9). Alternatively, these could be the locations of a set of interacting point objects and the goal could be to track their collective behavior over time and detect abnormalities [4]. 3D landmark shape sequences are often obtained from a time sequence of volume images, for example by manually or automatically extract landmarks from a 3D heart MR image sequence or from a time sequence of brain MRI volumes. 2D or 3D landmarks may also be obtained from motion capture (MOCAP) [6] data where sensors are attached to various joints of the human body and their 3D coordinates measured over time. The Carnegie Mellon Motion Capture database (CMU-MOCAP) is a common example. Modeling Mocap data has applications in bio-mechanics and graphics to understand the motion of human joints in various actions.

A shape activity model serves as the prior for model-based automatic tracking or filtering of landmark shape sequences. We demonstrate this in Sec. 5 and Fig. 8, 9 for human activity videos taken from CMU-MOCAP database. Additionally, as demonstrated in [7], it can also be used for model-based compression of the shape sequence and this is useful in greatly reducing the amount of data to be stored or transmitted across a network. A third application is in graphics to synthesize

- *N. Vaswani and S. Das are with the Department of Electrical and Computer Engineering, Iowa State University, Ames, IA, 50011. E-mail: samarjit,namrata@iastate.edu. Part of this paper appeared in [1], [2]. This work was partially funded by NSF grant ECCS 0725849* new sequences for animation or to extrapolate existing sequences, for e.g. see Fig. 10. A fourth key application is in model based change detection or abnormality detection problems, e.g. [8], [4] and Fig. 11.

1.1 Our Contributions and Related Work

The key *contribution* of this work is a novel approach to define a generative model for 2D and 3D nonstationary landmark shape sequences. The main idea is to compute the tangent space representation of the current shape in the tangent space at the previous shape. This can be referred to as the "shape velocity" vector since it quantifies the "difference" between two consecutive shapes projected into the tangent space at the first one. The coefficients of shape velocity along the orthogonal basis directions spanning the current tangent space ("shape speed") can be modeled using standard vector time series models. An important requirement in doing this is to ensure that the basis directions of the current tangent space are *aligned* with those of the previous one. For both 2D and 3D shape sequences, we use the tangent space projections defined in [9].

Note that we could have just defined the model for m-D landmark shape sequences and 2D or 3D would follow as special cases. But, we do not do this because 2D landmark shapes' modeling is much more efficient; a) the shape computation from preshapes can be done in closed form (see (2)) while m-D landmarks require solving an SVD; b) the Procrustes mean is also much more easily computed in 2D (see (1)) while m-D requires an iterative alternating minimization algorithm.

A second *contribution* of our work is demonstrating the use of our nonstationary model for (a) sequentially filtering noise-corrupted landmark configurations to compute Minimum Mean Procrustes Square Error (MMPSE) estimates of the true shape; (b) for tracking, i.e. for using the filtering to predict the locations of the landmarks at the current time and using this prediction for faster and more accurate landmarks' extraction from the current image; (c) for synthesis; (d) change detection. Most of our experiments focus on (a) and (b). Greatly improved performance of our tracking and filtering algorithm over existing work [10], [4], [8] is demonstrated. Due to the nonlinearities in the shape dynamics model and the non-Gaussian observation model (similar to that of Condensation [11]), we use a particle filter (PF) [12] for filtering and tracking. Our tracking problem is a typical example of a large dimensional problem with frequently multimodal observation likelihoods (due to background clutter and missing landmarks) and hence we replace the basic PF used in previous work by the recently proposed PF with Efficient Importance Sampling (PF-EIS). We demonstrate that PF-EIS has a much better performance for landmark shape tracking than the basic PF, when the number of particles used is small.

In recent years, there has been a large amount of work on modeling sequences of landmark shapes - both in statistics [9], [13] and in computer vision and medical image analysis [10], [11], [14], [15], [4], [8], [16], [17]. Active shape models (ASM) [10], also referred to as Point Distribution Models [18] is a most widely used model for landmark shapes. ASMs assume that shape belongs to a Euclidean space. But because of the scaling and rotation, the shape space is clearly non-Euclidean. The Euclidean assumption is valid only if all shapes in the sequence deviate by only a small amount from the mean shape. Recent work [4], [8] modeled the dynamics of stationary shape activities (SSA) in the tangent space to the mean shape. Because of the single mean shape assumption, this again cannot model large deviations from the mean (this is discussed in detail in Sec. 2.2.

But in most real applications, there is large shape variation over a long sequence and so a single mean shape plus an ASM or SSA model does not suffice. For e.g., consider a running sequence (see Fig. 8). Another example is the changes in shape within a single heart cycle. In existing work, the ASM is usually replaced by piecewise ASMs [19], for example different ASMs are used for systolic and diastolic motions in [19] or SSA is replaced by piecewise SSA [4]. Piecewise ASMs are good for recognition problems, but not for automatic tracking or for compression since they do not model the transitions between pieces well. When piecewise SSA was used for tracking in [20], it needed to use separate change detection and shape recognition procedures to detect when and which piece to switch to. In this work, we demonstrate through extensive experiments that both filtering and tracking using our model significantly outperforms either ASMs or SSAs.

Smoothing splines [13], [21] is, to the best of our knowledge, the only other existing work that truly models nonstationary landmark shape sequences (other than the piecewise models discussed above). But it does not provide a generative model for the shape sequences, which is the key requirement in tracking, compression or synthesis applications. Note that we briefly introduced the nonstationary model for 2D landmark shapes in [4]. But it had one major error - the tangent space basis directions were not aligned over time and as a result the model on their coefficients vector was wrong (we explain this issue in Sec. 2.3). No experiments were done with the model in [4] and hence this problem was never detected.

The key difference of our work from Condensation [11] is that Condensation only models and tracks global affine deformation between two landmark configurations. This is a valid model for rigid or approximately rigid object motion in front of an affine camera, but not for modeling shape change of different parts of the human body performing different activities/actions such as running or jumping or for activities of groups of interacting persons/vehicles (modeled as landmarks) where there is significant local shape deformation which is not affine.

Other related work include Active Appearance Models (AAM) [14] and Active Appearance Motion Models (AAMM) [15] both of which use joint models on appearance and shape change, while in the current work we focus only on models for shape change. A model on only shape change (not appearance) is invariant to intensity changes in the images e.g. large illumination changes or clothing change.

Also note that our dynamic model is similar in spirit to [22] where the authors use piecewise geodesic priors to define models for motion on Grassmann manifolds and use these models for time-varying subspace estimation using a particle filter.

There are many other representations of shape other than landmark shape, for e.g. Fourier descriptors [23], B-splines [24], angle function or curvature based representations [25], deformable snakes and level sets [26], and corresponding models for shape change.

The automatic tracking and landmark extraction technique developed in this work has direct applications to articulated human body tracking over videos/image sequences. Some other works in this area include [16], [17], [27], [28], [29]. Most of them use articulated body model directly for tracking purposes. Other related work also includes Gaussian process latent variable models GPVLM [16], [17] based approaches to define and to automatically learn the observation model parameters from training observed data [30].

In Sec. 2, we explain the nonstationary model for 2D landmark shape sequences and give the parameter estimation algorithm. We also explain the problems with SSA and ASM in detail. We discuss the modeling and parameter estimation for 3D shape sequences in Sec. 3. We describe the methodology for filtering out shapes from noisy observations and for tracking in Sec. 4. In Sec. 5 we describe our experiments and results. We conclude the paper in Sec. 6.

2 Modeling 2D Shape Sequences

For modeling human motion activity or any activity involving multiple interacting objects, we represent body joints/objects as the landmark points and the corresponding activity is represented as a sequence of deforming landmark shapes over time. It is done two steps. First, we transform the shape sequence to a vector time series using the nonstationary shape deformation model. Then we fit standard statistical models to the time series.

2.1 2D Landmark Shape Analysis Preliminaries

We use a discrete representation of shape of a group of K **landmarks**. The various moving objects (point objects) in a group activity or the rigid parts of human body in an action form the "landmarks" as shown in Fig. 8, 9. The **configuration** is the set of landmarks, in the 2D case it is the x and y coordinates of the landmarks which can be represented as a K dimensional complex vector [9].

The raw configuration is denoted as S. It can be normalized for translation (moving origin to the centroid of the configuration) and then for scale (normalizing the translation normalized vector by its Euclidean norm) to yield the **pre-shape**, denoted by w. The configuration of K points after translation normalization, denoted by y, lies in $\mathcal{C}^{K-1}$ ((K-1)-dimensional complex space) while the pre-shape, w, lies on a hyper-sphere in $\mathcal{C}^{K-1}$. A pre-shape w_1 can be aligned with another pre-shape w_0 by finding the rotation angle for the best fit (minimum mean square error fit) and this gives the **Procrustes fit** of w_1 onto w_0 [9]. This is the **shape** of w_1 w.r.t. w_0. The **Procrustes distance** between preshapes w_1 and w_0 is the Euclidean distance between the Procrustes fit of w_1 onto w_0. The **Procrustes mean** of a set of preshapes $\{w_i\}_{i=1}^N$ is the minimizer of the sum of squares of Procrustes distances from each w_i to an unknown unit size mean configuration μ [9]. As shown in [9], μ can be computed as the principal eigenvector of the pre-shape covariance matrix, i.e.

$$\mu = \arg \max_{u:||u||=1} u^*[\frac{1}{N}\sum_{i=1}^{N} w_i w_i^*]u \tag{1}$$

Any pre-shape of the set can then be aligned w.r.t. this procrustes mean to return the **shape** (denoted by z) w.r.t. the procrustes mean shape, μ [9].

The shape space, $\mathcal{M}$, is a manifold in $\mathcal{C}^{K-1}$ and hence its actual dimension is $\mathcal{C}^{K-2}$. Thus the tangent plane at any point of the shape space is a $\mathcal{C}^{K-2}$ dimensional hyperplane in $\mathcal{C}^{K}$ [9]. The projection of a configuration, S, in the tangent space at a pole, μ, is evaluated [9] as follows:

$$\begin{aligned} y &= C_K S, \ \ C_K \triangleq I_K - 1_K 1_K^T/K \\ w &= y/||y|| \\ \theta &= angle(w^*\mu), \ \ z = we^{j\theta} \end{aligned} \tag{2}$$

$$v(z,\mu) = [I_K - \mu\mu^T]z \tag{3}$$

Here, I_K is a $K \times K$ identity matrix and 1_K is a column vector with K rows with all entries as 1. The notation x^T denotes transpose for real vector x and x^* denotes conjugate transpose for complex vector x. The inverse map (projection from tangent space to shape space) is given by [9],

$$z = (1 - v^*v)^{\frac{1}{2}}\mu + v \tag{4}$$

2.2 Problem with SSA and ASM models

The Stationary Shape Activity (SSA) model proposed in [4] computed a single mean shape μ for a training sequence and aligned each preshape, w_t, in the sequence to μ to obtain the shape sequence z_t. Tangent projections, $v(z_t, \mu)$, of each z_t were computed in the tangent space at μ and their time series was modeled using an autoregressive (AR) model. The work of [8] replaced AR by ARMA models and used the models for recognition problems. The Active Shape Model (ASM) of [10] assumed that z_t belongs to a vector space and replaced the tangent space projection given in (3) by its linear version $v(z_t, \mu) = z_t - \mu$ and modeled the time series of $v(z_t, \mu)$.

Since both SSA and ASM assumed a single mean shape, they could model only small deviations from mean, which is only possible for stationary sequences. But in many applications, this assumptions may not hold, for example, a crawling or a dancing sequence or see Fig. 8. In these cases, the mean shapes for different time intervals are different. Or in other words, considering the entire sequence, the shape activity is essentially nonstationary. Now, if we force a fixed mean shape to such a deforming shape sequence, the resulting shapes, z_t, would drift too far away from μ. It is important to note that a single tangent space approximation works as long as each element of $v(z_t, \mu)$ for all shapes is less than 1 (otherwise the square root in (4) will be of a negative number). Also a time-invariant AR or ARMA model on $v(z_t, \mu)$'s is a valid one only if the magnitudes of each element of $v(z_t, \mu)$ are significantly smaller than 1 (this is because when $v(z_t, \mu)$ is large, i.e. when z_t is far from μ, small changes in $v(z_t, \mu)$ would correspond to very large changes in z_t). But for large shape variation, $v(z_t, \mu)$ will be large. In such a scenario, both SSA and ASM would fail to correctly model the shape dynamics.

2.3 Modeling Nonstationary Shape Sequences

To model a nonstationary shape sequence, we use $\mu = z_{t-1}$ at time t. Thus,

$$\begin{aligned} z_t &:= w_t \frac{w_t^* z_{t-1}}{|w_t^* z_{t-1}|} \\ v_t &:= v(z_t, z_{t-1}) = [I - z_{t-1} z_{t-1}^*] z_t \end{aligned} \tag{5}$$

The inverse map is given by

$$z_t = (1 - v_t^* v_t)^{\frac{1}{2}} z_{t-1} + v_t \tag{6}$$

Since the projection of z_{t-1} in the tangent space at z_{t-1}, $T_{z_{t-1}}$, is zero, v_t can be interpreted as the difference, $(z_t - z_{t-1})$, projected into $T_{z_{t-1}}$, i.e. it is the "shape velocity" at time t.

The translation, scale and rotation normalization in 2D removes 2 complex dimensions (4 real dimensions) and thus the shape space is a $K-2$ dimensional manifold in $\mathcal{C}^K$ and so the tangent space is a $K-2$ dimensional hyperplane in $\mathcal{C}^K$ [9]. Thus the shape velocity, v_t has only $K-2$ independent complex dimensions, i.e. it can be rewritten as $v_t = U_t \tilde{c}_t$ where the columns of $(U_t)_{K \times K-2}$ contain the $K-2$ orthonormal basis directions spanning $T_{z_{t-1}}$ and $\tilde{c}_t \in \mathcal{C}^{K-2}$ are the basis coefficients. $\tilde{c}_t$ may be interpreted as a "shape speed" vector.

Note that, by definition, $T_{z_{t-1}}$ is perpendicular to z_{t-1} and to 1_K. Also, z_{t-1} is perpendicular to 1_K (due to translation normalization). Thus the projection matrix for $T_{z_{t-1}}$ is $[I_K - z_{t-1} z_{t-1}^*] C_K = [I_K - z_{t-1} z_{t-1}^* - 1_K 1_K^T / K]$. In other words, U_t satisfies

$$U_t U_t^* = [I_K - z_{t-1} z_{t-1}^* - 1_K 1_K^T / K] \tag{7}$$

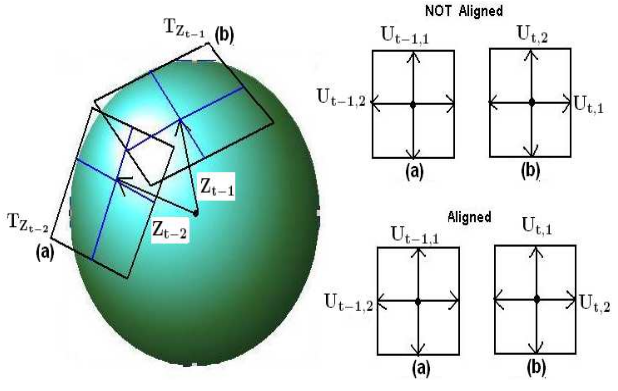

Fig. 1. This figure shows the alignment of successive tangent spaces for NSSA. When using [4], [1], the axes (here x and y) of the consecutive tangent planes may not be aligned (top). Our method gives aligned axes (bottom).

One way to obtain U_t is by computing the Singular Value Decomposition (SVD) of the right hand side (RHS) of (7) and setting the columns of U_t equal to the left singular vectors with nonzero singular values. Denote this operation by $U_t = left.singular.vectors(M(z_{t-1}))$ where,

$$M(z) \triangleq [I_K - zz^* - 1_K 1_K^T / K] \tag{8}$$

This was used in [1], [4]. But if this is done at each t, the columns of of U_t and U_{t-1} may not be aligned. As an extreme example consider the following. Let $K = 4$. It may happen that $U_{t-1} = \begin{bmatrix} 1 & 0 \\ 0 & 1 \\ 0 & 0 \\ 0 & 0 \end{bmatrix}$ and $U_t = \begin{bmatrix} 0.1 & 0.995 \\ 0.995 & -0.1 \\ 0 & 0 \\ 0 & 0 \end{bmatrix}$. In this case, it is obvious that the first column of U_t corresponds to the second column of U_{t-1} and vice versa for second column of U_t. Or, in other words, $\tilde{c}_{t,1}$ corresponds to $\tilde{c}_{t-1,2}$ and $\tilde{c}_{t,2}$ to $\tilde{c}_{t-1,1}$. Thus if SVD is used to obtain U_t at each t, the $\tilde{c}_t$'s cannot be assumed to be identically distributed and so it is incorrect to model them by an AR model, which assumes stationarity of $\tilde{c}_t$. Notice the large modeling error of this method (NSSA-unaligned) in Fig. 3(a).

We fix this problem as follows (also see Fig. 1). To obtain an aligned sequence of basis directions over time, we obtain the m^{th} column of U_t by starting with the m^{th} column of U_{t-1}, making it perpendicular to z_{t-1} (by subtracting $z_{t-1} z_{t-1}^*$) and then using Gram-Schmidt orthogonalization to also make the resulting vector perpendicular to the first $m-1$ columns of U_t (i.e. by further subtracting out $\sum_{j=1}^{m-1} (U_t)_j (U_t)_j^*$). This procedure can be summarized as:

$$\begin{aligned} U_t &= g(U_{t-1}, z_{t-1}),\ where \\ g(.)_m &\triangleq [I - z_{t-1}z_{t-1}^* - \sum_{j=1}^{m-1} g(.)_j g(.)_j^*](U_{t-1})_m, \\ & \forall m = 1, \dots (K-2) \end{aligned} \quad (9)$$

Here, $g(.)_m$ denotes the m^{th} columns of $g(U_{t-1}, z_{t-1})$. U_0 is initialized as $U_0 = left.singular.vectors(M(z_0))$.

Now, since the columns of U_t are aligned, it is fair to assume that $\tilde{c}_{t,j}$'s are identically distributed for each j over time. Since they are also temporally correlated, we model them by an autoregressive model with lag 1 (AR(1) model). For simplicity of notation, we first convert $\tilde{c}_t$ into a $2K-4$ dimensional real vector. We denote this operation by,

$$c_t = vec(\tilde{c}_t) \quad (10)$$

and the inverse operation (obtaining the complex vector) is denoted by $\tilde{c}_t = vec^{-1}(c_t)$. Thus, in summary, the dynamical model of the state $X_t = [U_t, z_t, c_t]$ is given by

$$\begin{aligned} c_t &= A_c c_{t-1} + \nu_{c,t},\ \nu_{c,t} \sim \mathcal{N}(0, \Sigma_c) \\ U_t &= g(U_{t-1}, z_{t-1}) \\ z_t &= (1 - c_t^T c_t)^{1/2} z_{t-1} + U_t vec^{-1}(c_t) \end{aligned} \quad (11)$$

The last equation follows from (4) and the fact that $v_t = U_t\tilde{c}_t$, $U_t^* U_t = I$ and $\tilde{c}_t^*\tilde{c}_t = c_t^T c_t$. The above model is initialized with

$$z_0 = w_0,\ U_0 = left.singular.vectors(M(z_0)),\ c_0 = 0 \quad (12)$$

In the above model, we assume that $\nu_{c,t}$ is i.i.d Gaussian. We verified this fact by computing the histogram corresponding to each of the scalar dimensions of $\nu_{c,t}$ over the entire sequence (one of them is shown in Fig. 2) from a training sequence.

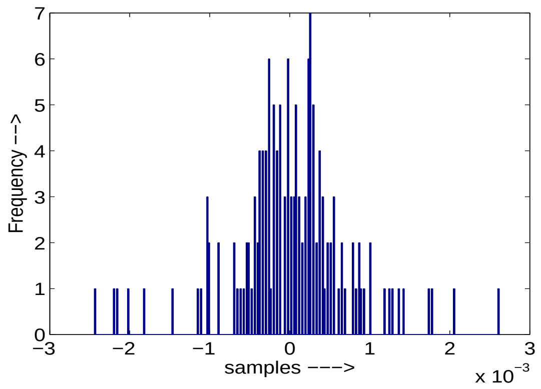

Fig. 2. This figure shows the histogram corresponding to one of the scalar dimensions of $\nu_{c,t}$ over the entire sequence. Similar results were found for other dimension as well. These results validate the fact why we can consider samples of $\nu_{c,t}$ as i.i.d Gaussian.

2.4 Model Parameter Estimation

The above model is completely specified by $z_{init} = w_0$, A_c, Σ_c. A_c is the AR transition matrix and Σ_c is the modeling error covariance matrix in the AR model. Given a training sequence of landmark configurations, $\{S_t\}_{t=0}^{N-1}$, a maximum-likelihood (ML) estimate of the parameters can be obtained as follows.

1) Obtain the shape sequence $\{z_t\}$ by translation, scale and rotation normalization of $\{S_t\}_{t=0}^{(N-1)}$ i.e. compute $y_t = C_K S_t$ and $w_t = \frac{y_t}{||y_t||}$ for each t. Set $z_0 = w_0$. Compute

$$z_t = w_t \frac{w_t^* z_{t-1}}{|w_t^* z_{t-1}|},\ \forall t > 0 \quad (13)$$

2) For all t, obtain the shape velocities $\{c_t\}$ from $\{z_t\}$. This involves computing

$$\begin{aligned} U_t &= g(U_{t-1}, z_{t-1}) \\ \tilde{c}_t &= U_t^* v_t = U_t^* z_t \\ c_t &= vec(\tilde{c}_t) \end{aligned} \quad (14)$$

starting with $U_0 = left.singular.vectors(M(z_0))$. The second equation above follows because $U_t^* v_t = U_t^*[I_K - z_{t-1}z_{t-1}^*]z_t = U_t^*[I_K - z_{t-1}z_{t-1}^* - 1_K 1_K^T/K]z_t = U_t^* U_t U_t^* z_t = U_t^* z_t$ (the second equality follows because z_t is translation normalized so that $1_K^T z_t = 0$ and third one follows because by definition, $U_t U_t^* = [I_K - z_{t-1}z_{t-1}^* - 1_K 1_K^T/K]$).

3) Obtain a maximum likelihood (ML) estimate of the AR model parameters, A_c, Σ_c, from $\{c_t\}$ by using the Yule-Walker equations, i.e.

$$\begin{aligned} A_c &= R_c(1) R_c(0)^{-1},\ where \\ R_c(0) &= \frac{1}{N}\sum_{t=0}^{N-1} c_t c_t^T,\ R_c(1) = \frac{1}{N-1}\sum_{t=1}^{N-1} c_t c_{t-1}^T \\ \Sigma_c &= \frac{1}{N-1}\sum_{t=1}^{N-1}(c_t - A_c c_{t-1})(c_t - A_c c_{t-1})^T \end{aligned} \quad (15)$$

2.4.1 Using Multiple Training Sequences

If more than one training sequence is available, one can compute a mean z_{init} (denoted by $\tilde{z}_{init}$) by aligning the initial preshapes, w_0, of all the sequences. We set z_0 for each sequence as the corresponding w_0 aligned to $\tilde{z}_{init}$. These operations make sure that the initial shapes of all the training sequences are aligned. Now, starting with z_0 we can obtain the the shape speed, c_t's for each sequence. Say, we have a total of q training sequences for a given motion activity, each with length N. We denote c_t's corresponding to the i^{th} sequence as $\{c_t^i\}$, where $i = 1, ..., q$. Now, we can estimate $R_c(0), R_c(1)$ as $R_c(0) = \frac{1}{q}\sum_{i=1}^{q}\frac{1}{N}\sum_{t=0}^{N-1} c_t^i c_t^{i\,T}$ and $R_c(1) = \frac{1}{q}\sum_{i=1}^{q}\frac{1}{N-1}\sum_{t=1}^{N-1} c_t^i c_{t-1}^{i\,T}$. Finally, we compute $A_c = R_c(1)R_c(0)^{-1}$ and $\Sigma_c = \frac{1}{q}\sum_{i=1}^{q}\Sigma_c^i$ where $\Sigma_c^i = \frac{1}{N-1}\sum_{t=1}^{N-1}(c_t^i - A_c c_{t-1}^i)(c_t^i - A_c c_{t-1}^i)^T$. The entire procedure is summarized in Algorithm 1.

Algorithm 1 **2D NSSA: Training with Multiple Training Sequences For a Given Motion Activity**

```
Input: Pre-shapes corresponding to $q$ training sequences ($\{w_t^i\}_{t=0}^{N-1}$, $i = 1, ..., q$)
Objective: To learn the parameters $[\tilde{z}_{init}, A_c, \Sigma_c]$.

Start: Compute $\tilde{z}_{init} = \mu(w_0^1, w_0^2, ..., w_0^q,)$ where, $\mu(.)$ is computed using (1). It given the procrustes mean shape of $\{w_0^i\}_{i=1}^q$. Compute $\tilde{U}_{init} = left.singular.vectors(M(\tilde{z}_{init}))$ where, M(.) is given in equation (8)

1) For $i = 1$ through $q$ do
    a) Compute $z_0^i = w_0^i \frac{{w_0^i}^* \tilde{z}_{init}}{|{w_0^i}^* \tilde{z}_{init}|}$
    b) Compute $U_0^i = g(\tilde{U}_{init}, z_0^i)$ and set $c_0^i = 0$
    c) For $t$ = 1 through $(N-1)$, do
        Set $z_t^i = w_t^i \frac{{w_t^i}^* z_{t-1}^i}{|{w_t^i}^* z_{t-1}^i|}$
        Set $U_t^i = g(U_{t-1}^i, z_{t-1}^i)$
        Set $c_t^i = vec({U_t^i}^* z_t^i)$
2) Compute $A_c = R_c(1)R_c(0)^{-1}$ where $R_c(0) = \frac{1}{q}\sum_{i=1}^q \frac{1}{N}\sum_{t=0}^{N-1} c_t^i {c_t^i}^T$ and $R_c(1) = \frac{1}{q}\sum_{i=1}^q \frac{1}{N-1}\sum_{t=1}^{N-1} c_t^i {c^i}_{t-1}^T$
3) Compute $\Sigma_c = \frac{1}{q}\sum_{i=1}^q = \frac{1}{N-1}\sum_{t=1}^{N-1}(c_t^i - A_c c_{t-1}^i)(c_t^i - A_c c_{t-1}^i)^T$
```

3 Modeling 3D Shape Sequences

A 3D configuration is represented by a set of K ordered landmarks as a $(K \times 3)$ matrix whose each row corresponds to the (x, y, z) coordinates of the corresponding landmark. In this section, we discuss the basics of 3D landmark shape analysis [9] and then develop 3D non-stationary shape activity model (3D-NSSA).

3.1 3D Landmark Shape Analysis Preliminaries

For 3D shapes, the computation of pre-shape $(w)_{K\times 3}$ from raw shape $(S)_{K\times 3}$ is similar to the 2D case i.e. first get the centered shape $(y)_{K\times 3}$ and then perform size normalization.

$$\begin{aligned} y &= C_K S \quad \text{where, } C_K \text{ is given in (2)} \\ w &= \frac{y}{||y||_F} \end{aligned} \tag{16}$$

Here, $||.||_F$ denotes *Frobenius norm* of a matrix. The rotation aligned shape z is obtained from pre-shape w in the following way. Say, we want to align $(w)_{K\times 3}$ w.r.t $(\mu)_{K\times 3}$. We do this as :

$$\begin{aligned} z &= w\mathcal{U}\mathcal{V}^T \quad \text{where,} \\ \mathcal{V}\Lambda\mathcal{U}^T &= SVD(\mu^T w) \end{aligned} \tag{17}$$

$\mathcal{V}$,$\mathcal{U}$ are the left and right singular vectors of the 3×3 matrix $(\mu^T w)$. Another important thing about 3D shape analysis is the vectorization operation [9]. Say, $\mathbf{z}$ is the shape at a given instant which is a $(K \times 3)$ matrix with columns $\mathbf{z_1}, \mathbf{z_2}, \mathbf{z_3}$. We vectorize $\mathbf{z}$ to a $3K$ length vector as follows.

$$vec_{3D}(\mathbf{z}) = (\mathbf{z_1^T}, \mathbf{z_2^T}, \mathbf{z_3^T})^T \tag{18}$$

The inverse operation is given by $vec_{3D}^{-1}(.)$ which forms a $K \times 3$ matrix from a $3K$ length vector. The tangent space coordinate $v(z, \mu)$ of a shape z w.r.t the shape μ is given as follows,

$$v(z, \mu) = [I_{3K} - vec_{3D}(\mu)vec_{3D}(\mu)^T]vec(z) \tag{19}$$

The inverse map (i.e. from tangent space to shape space) is given as,

$$z = vec_{3D}^{-1}((1 - v^T v)^{\frac{1}{2}} vec_{3D}(\mu) + v) \tag{20}$$

3.2 3D Nonstationary Shape Activity (3D-NSSA)

To define an NSSA model on 3D shape data, we first obtain the translation and scale normalized pre-shape sequence $\{w_t\}$ from the 3D configuration sequence $\{S_t\}$ using (16). As in the 2D case, we use $\mu = z_{t-1}$ to compute the shape sequence followed by computing the shape velocity and shape speed vectors in an exactly analogous fashion. The final procedure can be summarized as follows.

First, we have $z_{init} = z_0 = w_0$ and then we compute the initial tangent space basis matrix as $U_{init} = U_0 = left.singular.vectors(M_{3D}(z_0))$ where,

$$M_{3D}(z) \triangleq [I_{3K} - vec(z)vec(z)^T]C_{K,3D} \tag{21}$$

where, $C_{K,3D} = \begin{bmatrix} C_K & \mathbf{0_{K\times K}} & \mathbf{0_{K\times K}} \\ \mathbf{0_{K\times K}} & C_K & \mathbf{0_{K\times K}} \\ \mathbf{0_{K\times K}} & \mathbf{0_{K\times K}} & C_K \end{bmatrix}$. Here, $\mathbf{0_{K\times K}}$ is a $(K \times K)$ matrix with all zero entries and C_K is defined in (2). Now starting with z_0 and U_0, the computation of the corresponding time sequence of *shape speed* vectors is done as follows,

$$\begin{aligned} z_t &= w_t\mathcal{U}\mathcal{V}^T, \; where \; \mathcal{V}\Lambda\mathcal{U}^T = SVD(z_{t-1}^T w_t) && (22) \\ U_t &= g(U_{t-1}, vec_{3D}(z_{t-1})) && (23) \\ c_t &= U_t^T v_t = U_t^T vec_{3D}(z_t) && (24) \end{aligned}$$

where, $g(.)$ is defined in (9). The reason why $U_t^T v_t = U_t^T vec_{3D}(z_t)$ is similar to the 2D case (see discussion below equation (14)).

We model c_t using a first order AR model (in general this may be replaced by any appropriate model for c_t).

Thus, the forward model for generating a 3D shape sequence is:

$$\begin{aligned} c_t &= A_c c_{t-1} + n_t,\ n_t \sim \mathcal{N}(0, \Sigma_c) \\ U_t &= g(U_{t-1}, vec_{3D}(z_{t-1})) \\ z_t &= vec_{3D}^{-1}((1 - c_t^T c_t)^{\frac{1}{2}} vec_{3D}(z_{t-1}) + U_t c_t) \end{aligned} \quad (25)$$

The last equation follows from (20) and the fact that $v_t^T v_t = (U_t c_t)^T U_t c_t = c_t^T (U_t^T U_t) c_t = c_t^T c_t$ and $U_t^T U_t = I$.

3.3 Model Parameter Estimation

The parameter estimation algorithm for the 3D case can be summarized as follows.

1) For all t, obtain $\{w_t\}$ from a given 3D landmark configuration sequence, $\{S_t\}$.
2) For all t, compute $\{z_t\}$ from $\{w_t\}$ using (22).
3) For all t, compute $\{c_t\}$ from $\{z_t\}$ using (23) and (24).
4) Estimate the AR model parameters for c_t using the Yule-Walker equations given in (15).

4 Filtering and Tracking

The goal of filtering is to filter out the noise and get a good estimate of the true landmark shape from noisy observed landmarks. In our algorithm, the particle filter takes noisy observed landmark data as input and outputs the Minimum Mean Procrustes-distance Squared Error (MMPSE) estimate of the true landmark shape. The MMPSE estimate of shape can be derived by following the procrustes mean derivation [9] as,

$$\begin{aligned} \hat{z}_t &= \arg\min_{\mu} E[d^2(z_t, \mu)|Y_{1:t}] \\ &= \arg\min_{\mu} E[||z_t z_t^* \mu - \mu||^2 | Y_{1:t}] \\ &= \arg\max_{\mu} \mu^* E[z_t z_t^* | Y_{1:t}] \mu \end{aligned} \quad (26)$$

where $E[\cdot|Y_{1:t}]$ denotes the conditional expectation given $Y_{1:t}$, d denotes the Procrustes distance [9] and $Y_{1:t}$ are the observations until t. The last equality follows because $z_t^* z_t = 1$ and $\mu^* \mu = 1$. Under a particle filtering setup the MMPSE estimate is computed as, $\hat{z}_t$ = principal eigenvector of $\sum_{i=1}^{N_{pf}} z_t^i z_t^{i*} w_t^i$ where N_{pf} denotes number of particles, i denotes the i^{th} particle and w_t^i represents the importance weight corresponding to the i^{th} particle i.e. $p(z_t|Y_{1:t}) \approx \sum_{i=1}^{N_{pf}} w_t^i \delta(z_t - z_t^i)$. The configuration parameters i.e. scale, translation and rotation are also estimated in the process of filtering. Apart from removing random additive noise, particle filtering can also be used to 'clean up' the effects of occlusion and clutter.

Tracking is used to extract and filter out landmark configurations from a sequence of images. Filtering plays a very crucial role in the process. In fact, tracking can be considered as observation extraction coupled with filtering. It works as follows. A shape deformation model (as described in Sec. 2.3) predicts the shape at the current instant using the previous shape estimates. Similarly, scale, translation and rotation models are used to predict their values as well. These, coupled with the predicted shape, gives the predicted landmark locations (i.e. predicted configuration) at the current instant. Using these predicted landmark locations in the current image, the landmarks can be extracted for the current image using any technique, for e.g. edge detection or optical flow. Our method for doing this is described in Algorithm. 4 and Sec. 4.5. Once the observed landmarks are obtained, they are filtered to get a MMPSE estimate of the true landmark shape and MMSE estimates of scale, rotation and translation. These estimates are again utilized to extract the observed landmark locations at the next time instant as described above.

We describe our state transition model and observation model in Sec. 4.1 and 4.2. We discuss our choice of PF algorithms and their application to our problem in Sec. 4.3 and 4.4 respectively. The PF-based tracking algorithm to extract landmarks from video sequences is described in Sec. 4.5.

4.1 System Model (State Transition Model)

Since the observations are landmark configurations, to extract them, we need to estimate both the shape and the "motion" (scale, translation and rotation). Thus our state vector is, $X_t = [s_t, \theta_t, \tau_t, c_t, z_t, U_t]$ where s_t is the logarithm of global scale, θ_t is the global rotation, τ_t is the xy translation, c_t is the shape speed vector, z_t is the shape and U_t is the basis set spanning the current tangent space. The shape dynamics model is given in (11). It is a second order model on z_t which is equivalent to a first order model on the shape speed c_t. We use a first order model on logarithm of global scale, s_t, global 2D rotation θ_t (this typically models the random motion of camera) and translation τ_t.

$$\begin{aligned} s_t &= \alpha_s s_{t-1} + \nu_{s,t},\ \nu_{s,t} \sim \mathcal{N}(0, \sigma_s^2) \\ \theta_t &= \theta_{t-1} + \nu_{\theta,t},\ \nu_{\theta,t} \sim \mathcal{N}(0, \sigma_\theta^2) \\ \tau_t &= \tau_{t-1} + \nu_{\tau,t},\ \nu_{\tau,t} \sim \mathcal{N}(0, \sigma_\tau^2) \end{aligned} \quad (27)$$

Note that in case of filtering (when landmark observations are already available), translation can be normalized for. Since it is a linear process the form of the observation noise pdf does not change. But in case of tracking to predict and extract landmarks from image sequences, translation does need to be tracked to predict where the configuration of landmarks translated to.

The resulting state transition prior becomes,

$$\begin{aligned} p(X_t|X_{t-1}) = \ & \mathcal{N}(\alpha_s s_{t-1}, \sigma_s^2) \mathcal{N}(\theta_{t-1}, \sigma_\theta^2) \times \\ & \mathcal{N}(\tau_{t-1}, \sigma_\tau^2) \mathcal{N}(A_c c_{t-1}, \Sigma_c) \times \\ & \delta(U_t - g(U_{t-1}, z_{t-1})) \delta(z_t - f(z_{t-1}, U_t, c_t)) \end{aligned}$$

where δ denotes the Dirac delta function and $f(z_{t-1}, U_t, c_t) \triangleq (1 - c_t^T c_t)^{1/2} z_{t-1} + U_t vec^{-1}(c_t)$ and $g(.)$ is defined in (9).

Algorithm 2 **PF-Gordon for Landmark Shape Filtering**

```
Initialization: At time $t = 0$, sample $s_0^{(i)} \sim \mathcal{N}(s_0, \sigma_s^2)$, $\theta_0^{(i)} \sim \mathcal{N}(\theta_0, \sigma_\theta^2)$, $c_0^{(i)} = \mathbf{0}$, $z_0^{(i)} = z_0$ and $U_0^{(i)} = U_0$. Here, $i = 1, ..., N_{pf}$ where, $N_{pf}$ is the number of particles.
For $t > 0$,
    1) Importance sample $X_t^{(i)} \sim p(X_t|X_{t-1}^{(i)})$ as $s_t^i \sim \mathcal{N}(\alpha_s s_{t-1}^i, \sigma_s^2)$, $\theta_t^i \sim \mathcal{N}(\alpha_\theta \theta_{t-1}^i, \sigma_\theta^2)$, $c_t^i \sim \mathcal{N}(A_c c_{t-1}^i, \Sigma_c)$, $U_t^i = g(U_{t-1}^i, z_{t-1}^i)$, $z_t^i = f(z_{t-1}^i, U_t^i, c_t^i)$. $i = 1, 2, ..., N_{pf}$
    2) Weight and Resample. Compute $w_t^i = \frac{\tilde{w}_t^i}{\sum_{j=1}^{N_{pf}} \tilde{w}_t^j}$ where, $\tilde{w}_t^i = w_{t-1}^i p(Y_t|X_t^i)$ with, $p(Y_t|X_t^i) = p(Y_t|h(s_t^i, \theta_t^i, z_t^i)) = \prod_{k=1}^K [(1-p)\mathcal{N}([h(s_t^i, \theta_t^i, z_t^i)]_k, \sigma_o^2) + p\mathcal{N}(0, 100\sigma_o^2)]$, $\forall i$
    3) Compute the MMPSE estimate $\hat{z}_t$ as the principal eigenvector of $\sum_{i=1}^{N_{pf}} z_t^i z_t^{i*} w_t^i$. Estimate configuration parameters as $\hat{s}_t = \sum_{i=1}^{N_{pf}} w_t^i s_t^i$ and $\hat{\theta}_t = \sum_{i=1}^{N_{pf}} w_t^i \theta_t^i$
    4) Set $t \leftarrow t + 1$ and go to step 1.
```

4.2 Observation Model

There are various ways to extract landmarks from image sequences - e.g. edge detection followed by extracting the K strongest edges closest to predicted landmark locations or using the KLT [31] (block optical flow estimation) algorithm at or around predicted landmark locations. As explained in Sec. 4.5 and Algorithm. 4, we use a modification of KLT for this purpose.

The configuration of landmarks is obtained from the shape, scale and rotation by the transformation $h(s_t, \theta_t, z_t) = z_t e^{s_t} e^{j\theta_t}$. The simplest observation model is of the form

$$Y_t = h(s_t, \theta_t, z_t) + w_t, \;\; w_t \sim \mathcal{N}(0, \sigma_o^2 I) \tag{28}$$

where w_t is a complex Gaussian noise vector. This assumes that there is no background clutter: each of the K strongest edges or the K KLT-feature points are always generated by the true landmark location plus some error modeled as Gaussian noise. But this is often a simplistic model since there is always background clutter that generates false edges or false KLT-feature matches or there might be missing landmarks due to blur or occlusion. Thus it may happen that out of the K "observed landmark locations", some landmark at some time is actually generated by clutter (e.g. if a true landmark is blurred or occluded, while a nearby clutter point has a stronger edge). We model this as follows: with a small probability p, the k^{th} landmark, $Y_{t,k}$, is generated by a clutter point (model a clutter point location as a large variance Gaussian or by a uniform), independent of other landmarks. With probability $(1-p)$ it is generated by a Gaussian noise-corrupted actual landmark (independent of other landmarks), i.e.

$$Y_{t,k} \sim (1-p)\mathcal{N}([h(s_t, \theta_t, z_t)]_k, \sigma_o^2) + p\mathcal{N}(0, 100\sigma_o^2) \tag{29}$$

The above model has been adapted from the observation model used in Condensation [11]. The resulting observation likelihood term is,

$$p(Y_t|X_t) = \prod_{k=1}^{K} (1-p)\mathcal{N}([h(s_t, \theta_t, z_t)]_k, \sigma_o^2) + p\mathcal{N}(0, 100\sigma_o^2)$$

4.3 Particle filter with Efficient Importance Sampling

The first PF algorithm, PF-Gordon [12], used the state transition prior (i.e. $p(X_t|X_{t-1})$) as the importance density. This assumes nothing and has very small computation burden per particle. But since it does not use knowledge of the current observation, the weights variance can be large, particularly when the observations are more reliable than the prior model. Thus it requires more particles for a given accuracy level compared to the case when the knowledge of observations are used. The optimal importance density [32] is given by the posterior conditioned on the previous state, denoted by p^* where,

$$p^*(X_t) \triangleq p(X_t|X_{t-1}, Y_t) \tag{30}$$

But in most problems, including ours, p^* cannot be computed analytically. When it is unimodal, PF-Doucet [32] approximates it by a Gaussian about its mode (Laplaces approximation [33]) and samples from the Gaussian. Other work that also implicitly assume that p^* is unimodal includes [34], [35]. But in our case, the observation likelihood is a raised Gaussian as a function of $[h(.)]_k$, and is thus heavy tailed. If the equivalent state transition prior of $[h(.)]_k$ is broad (e.g. this will happen if STP of s_t or θ_t is broad), whenever $Y_{t,k}$ is generated from the outlier distribution (i.e. is far from the predicted landmark location), the resulting posterior given the previous state, $p^*(X_t) \triangleq p(X_t|X_{t-1}, Y_t)$ will be multimodal.

For such problems where p^* is often multimodal, particle filter with efficient importance sampling (PF-EIS) was proposed in [36] which combines the ideas of both PF-Gordon and PF-Doucet to handle multimodal observation likelihoods. This algorithm relies on the fact that even though p^* is multimodal, for most real-life problems it is possible to split the state vector X_t into an "effective basis" $X_{t,s}$ and "residual space" $X_{t,r}$ in such a way that p^*, conditioned on $X_{t,s}$, is unimodal i.e.

$$p^{**,i}(X_{t,r}) \triangleq p^*(X_t|X_{t,s}^i) = p(X_{t,r}|X_{t-1}^i, X_{t,s}^i, Y_t) \tag{31}$$

is unimodal. Here, the index i represents the sample from the i^{th} particle. We sample the $X_{t,s}$ particle, $X_{t,s}^i$, from its state transition prior (STP) but use Laplace's approximation [33], [32] to approximate $p^{**,i}$ by a Gaussian and sample $X_{t,r}$ from it. Thus we sample $X_{t,r}^i$ from

Algorithm 3 **PF-EIS for Landmark Shape Filtering**

```
Initialization: At time $t=0$, sample $s_0^{(i)} \sim \mathcal{N}(s_0,\sigma_s^2)$, $\theta_0^{(i)} \sim \mathcal{N}(\theta_0,\sigma_\theta^2)$, $c_0^{(i)} = \mathbf{0}$, $z_0^{(i)} = z_0$ and $U_0^{(i)} = U_0$. Here, $i = 1, ..., N_{pf}$ where, $N_{pf}$ is the number of particles.
For $t > 0$,
    1) Importance sample $s_t^i \sim \mathcal{N}(\alpha_s s_{t-1}^i, \sigma_s^2)$, $\theta_t^i \sim \mathcal{N}(\alpha_\theta \theta_{t-1}^i, \sigma_\theta^2)$. $i = 1, 2, ..., N_{pf}$
    2) Compute $m_t^i = \arg\min_{c_t} L^i(c_t)$ and $\Sigma_{IS}^i = [\nabla^2 L^i(m_t^i)]^{-1}$ where $L^i$ is defined in (33).
    3) Importance sample $c_t^i \sim \mathcal{N}(m_t^i, \Sigma_{IS}^i)$. Compute $U_t^i = g(U_{t-1}^i, z_{t-1}^i)$ and $z_t^i = f(z_{t-1}^i, U_t^i, c_t^i)$.
    4) Compute Importance weights as, $w_t^i = \frac{\tilde{w}_t^i}{\sum_{j=1}^{N_{pf}} \tilde{w}_t^j}$ where, $\tilde{w}_t^i = w_{t-1}^i \frac{p(Y_t|h(s_t^i,\theta_t^i,z_t^i))\mathcal{N}(c_t^i;A_c c_{t-1}^i,\Sigma_c)}{\mathcal{N}(c_t^i;m_t^i,\Sigma_{IS}^i)}$.
    5) Compute the MMPSE estimate $\hat{z}_t$ as the principal eigenvector of $\sum_{i=1}^{N_{pf}} z_t^i z_t^{i*} w_t^i$. Resample.
    6) Set $t \leftarrow t+1$ and go to step 1.
```

$\mathcal{N}(m_t^i, \Sigma_{IS}^i)$ where

$$m_t^i = \arg\min_{X_{t,r}}[-\log p^{**,i}(X_{t,r})] = \arg\min_{X_{t,r}} L^i(X_{t,r})$$
$$\Sigma_{IS}^i = [\nabla^2 L^i(m_t^i)]^{-1} \quad where$$
$$L^i(X_{t,r}) \triangleq [-\log p(Y_t|X_{t,s}^i, X_{t,r})] + [-\log p(X_{t,r}|X_{t-1}^i, X_{t,s}^i)]$$

and $\mathcal{N}(\mu, \Sigma)$ denotes a gaussian pdf with mean μ and covariance matrix Σ. As shown in [36], unimodality of $p^{**,i}$ is ensured if the variance of state transition prior (STP) of $X_{t,r}$ is small enough compared to distance between the modes of OL given $X_{t,s}$ in any direction. Even if $X_{t,s}$ is chosen so that this holds for most particles, at most times, the proposed algorithm will work.

4.4 PF-Gordon and PF-EIS for our problem

We summarize the basic PF (i.e. PF-Gordon [12]) for landmark shape filtering in Algorithm. 2. In order to develop the PF-EIS, we follow the steps as explained in Sec. 4.3. The choices of $X_{t,s}$ and $X_{t,r}$ under this problem set-up are justified as follows. Since the STP of s_t, θ_t is usually broad (to allow for occasional large camera motion or zoom), we use $X_{t,s} = [s_t, \theta_t]$ and $X_{t,r} = [c_t, z_t, U_t]$. Note that for the purpose of importance sampling only s_t, θ_t, c_t are the "importance sampling states" since z_t, U_t are deterministically computed from c_t and X_{t-1}. The particles of $X_{t,s}$ are sampled from its state transition prior, i.e. using the first two equations of (27). Conditioned on the sampled scale and rotation, $X_{t,s}^i$, it is much more likely that p^* is unimodal, i.e. $p^{**,i}(c_t, U_t, z_t)$ defined below is unimodal

$$p^{**,i}(c_t, z_t, U_t) = \zeta \; p(\; Y_t \mid h(s_t^i, \theta_t^i, z_t)\;)\; \mathcal{N}(c_t; A_c c_{t-1}^i, \Sigma_c) \times \delta(U_t - g(U_{t-1}^i, z_{t-1}^i))\delta(z_t - f(z_{t-1}^i, U_t, c_t))$$

where $\mathcal{N}(x;\mu,\Sigma)$ denotes the value of a Gaussian pdf with mean μ and variance Σ computed at the point x and ζ is a proportionality constant. Since the pdfs of U_t, z_t, conditioned on c_t, X_{t-1}, are Dirac delta functions, the above simplifies to:

$$\begin{aligned} p^{**,i} &= \zeta \; p(\; Y_t \mid h(s_t^i, \theta_t^i, f(z_{t-1}^i, g^i, c_t))\;)\; \mathcal{N}(c_t; A_c c_{t-1}^i, \Sigma_c) \times \\ &\quad \delta(U_t - g^i)\; \delta(z_t - f(z_{t-1}^i, g^i, c_t)) \\ &\triangleq p^{**,i}(c_t) \quad \delta(U_t - g^i)\; \delta(z_t - f(z_{t-1}^i, g^i, c_t)) \end{aligned} \tag{32}$$

where, $g^i \triangleq g(U_{t-1}^i, z_{t-1}^i)$. The importance sampling part of $X_{t,r}$ is only c_t. We compute the importance density for c_t by approximating $p^{**,i}(c_t)$ by a Gaussian at its unique mode. The mode is computed by minimizing $L^i(c_t) = -\log p^{**,i}(c_t)$ defined below

$$\begin{aligned} L^i(c_t) = [-\log p(\; Y_t \mid h(s_t^i, \theta_t^i, f(z_{t-1}^i, g^i, c_t))\;)] + \\ [-\log \mathcal{N}(\; c_t; A_c c_{t-1}^i, \Sigma_c\;)] \end{aligned} \tag{33}$$

The PF-EIS algorithm for landmark shape tracking is summarized in Algorithm. 3.

4.5 Tracking to Automatically Extract Landmarks

In this section we describe out technique to track and automatically extract landmark configurations over a sequence of images or a video. The system comprises of a optical-flow (OF) tracker coupled with filtering. We compute optical flow at a cluster of points around each currently estimated landmark location, $[\hat{S}_t]_k$ (k denotes k^{th} landmark) and use this to move the cluster of points into the next frame (frame $t+1$). The centroid of the moved cluster serves as the new observation for the k^{th} landmark at $t+1$. Same thing is done for all landmark points to get Y_{t+1} (the vector of observed landmark locations a $t+1$). This observation is fed into the NSSA-based PF which outputs the estimated landmark locations (and estimated shape) at $t+1$. The entire procedure is summarized in Algorithm. 4. For computing the optical flow we used the code/method developed by [37].

5 Experimental Results

We began by comparing the ability of NSSA to model real-life landmark shape sequences with that of SSA, ASM and the wrong NSSA model (NSSA-unaligned) [1]. This is discussed in Sec. 5.1. It was observed that NSSA had much smaller modeling error than all three. This comparison gave us the first indication that NSSA would provide a much more accurate prior dynamic model for Bayesian filtering or tracking applications, as well as also for synthesis/extrapolation applications.

Next we simulated multiple realizations of a "non-stationary shape activity" along with scale and rotation variations and attempted to track it using three different PF algorithms: the original PF (PF-Gordon) was compared with PF-Doucet [32] and PF-EIS [36] (described in Sec. 4.3). These comparisons are discussed in Sec.

Algorithm 4 **Automatic Landmark Extraction over a Sequence of Images**

```
Input: image(t-1), image(t), $\hat{S}_{t-1}$ (estimated landmark configuration at $t-1$)
Output: $\{X_t^i, w_t^i\}, i = 1, 2, ..., \hat{S}_t = \sum_{i=1}^{N_{pf}} (z_t^i e^{s_t^i + j\theta_t^i} + \tau_t^i) w_t^i$ (estimated landmark configuration at time t) where, $z_t$ is the shape and $e^{s_t}$, $\theta_t$, $T_t$ are the global scale, rotation and translation respectively.
1) For each estimated landmark $[\hat{S}_{t-1}]_k, k = 1, 2, \ldots K$, compute optical flow at a cluster of points around $[\hat{S}_{t-1}]_k$ and use this to move the points into image(t). Use the centroid of the moved cluster as the $k^{th}$ observed landmark at time $t$, $[Y_t]_k$. Do this for all landmark points to get $Y_t$
2) Run PF-Gordon using $Y_t$, i.e. implement steps 1 and 2 of Algorithm. 2. But this time, we include the global translation in the state-space as well.
3) Display the estimated landmarks' location, $\hat{S}_t = \sum_{i=1}^{N_{pf}} (z_t^i e^{s_t^i + j\theta_t^i} + \tau_t^i) w_t^i$ (estimated landmark configuration at time $t$), set $t \leftarrow t + 1$, and go to step 1.
```

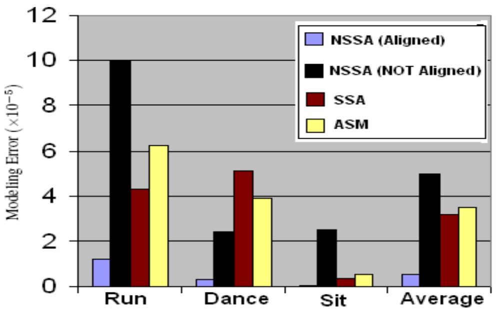

(a) 2D Modeling error

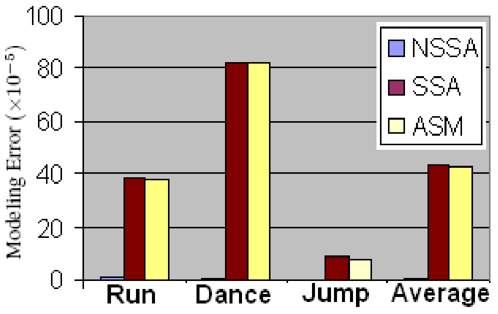

(b) 3D Modeling error

Fig. 3. Fig. 3(a) shows the modeling error(ME) for NSSA, ASM and ASM for a few activities using 2D MOCAP data. It is important to note that NSSA, without the basis alignment has a very large modeling error. While after the basis alignment is taken into account, NSSA has much lower ME than SSA and ASM. In Fig. 3(b) we show modeling error(ME) for NSSA, ASM and ASM for a few activities using 3D MOCAP data. Again NSSA had much lower ME compared to that SSA and ASM. That is why the corresponding bar plot for NSSA modeling error has almost disappeared.

5.2. It was observed that when the number of available particles is small, PF-EIS has the best performance.

Since most existing work that used SSA or ASM for tracking used PF-Gordon, we retained this PF for most of our comparisons between NSSA, SSA and ASM. The following four sets of experiments were done. In Sec. 5.3, we demonstrate the superior ability of NSSA-based PF (PF-Gordon with $N_{pf} = 1000$ and PF-EIS with $N_{pf} = 50$) to filter out the landmark shapes from heavily noise-corrupted and cluttered observed landmark configurations. In Sec. 5.4, we compare the tracking ability of NSSA-based PF with SSA-based PF and ASM-based PF, i.e. their ability to accurately extract out landmarks from image sequences. Once again NSSA is found to be significantly superior to SSA and ASM and also to direct landmark extraction (without any model-based filtering). The use of 3D-NSSA to accurately synthesize new human activity sequences is discussed in Sec. 5.5. In Sec. 5.6 we give a preliminary experiment that demonstrates that NSSA is able to remain in track even when a model change occurs.

5.1 Modeling Error Comparison

We used the Carnegie Mellon Motion Capture (CMU Mocap) database [6] for our experiments. Each file in the database had the coordinates of the markers placed at the body landmark locations (especially the body joints) for successive frames of a specific human motion activity e.g. running, jumping etc. An example is shown in Fig. 8. The corresponding 2D and 3D landmark shape sequences were used as the training data for learning the NSSA (or SSA or ASM) model parameters.

We define modeling error (ME) as the trace of the noise covariance matrix of the AR modeling error, i.e. ME = $trace(\Sigma_c)$, where $\Sigma_c = E[(c_t - A_c c_{t-1})(c_t - A_c c_{t-1})^T]$ and c_t are the "aligned" coefficients of shape velocity. We also compute the modeling error when the c_t's are not aligned, i.e. when U_t is computing using SVD at each t (as in [1]). When computing error for SSA, c_t are the tangent space coefficients of shape (not of shape velocity), i.e. all shapes z_t are projected into a single tangent space at the common mean shape μ. For ASM, modeling error is still the same but now $c_t = z_t - \mu$, i.e. the shape space is assumed to be Euclidean.

We computed the modeling error of SSA, ASM and NSSA (unaligned) for various human actions and compared with that of NSSA. It was found that NSSA has much lower modeling error than all three. The modeling error bar plot of 2D and 3D shape sequences has been shown in Fig. 3(a), 3(b) for a few motion activities.

Modeling error tells us how well we are able to capture the shape deformation dynamics using the given model. It thus quantifies how well we can predict the shape at

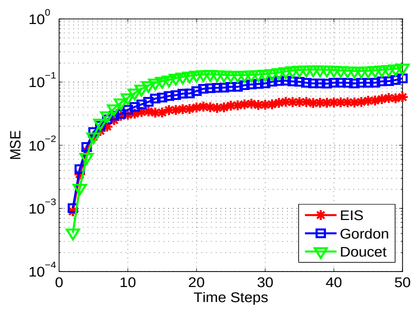

(a) Comparing PF algorithms

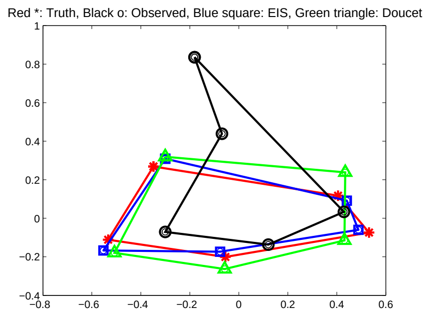

(b) PF-Doucet out of track

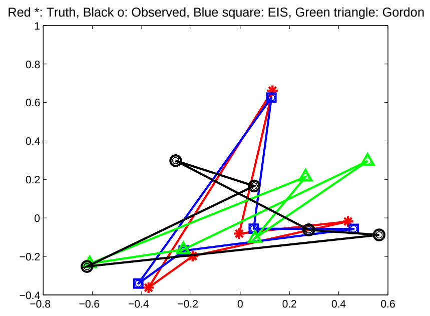

(c) PF-Gordon out of track

Fig. 4. In Fig. 4(a), we compare the MSE of of estimated configurations computed using PF-EIS, PF-Doucet and PF-Gordon for simulated shape sequence. EIS has the smallest MSE (discussed in Sec. 5.2). Fig. 4(b), 4(c): Examples where PF-Doucet, PF-Gordon lose track but PF-EIS does not.

a time instant given the information from the previous time instant. Thus Lower modeling error will result in better tracking ability and also a better ability to synthesize a new sequence or to extrapolate an existing sequence (graphics problems).

5.2 Comparing PF algorithms

We simulated landmark shape change of a set of $K = 5$ landmarks (a deforming pentagon) and tracked it using PF-EIS (Algorithm. 3), PF-Gordon (Algorithm. 2) [12] and PF-Doucet [32] with $N_{pf} = 50$ particles. The initial shape, z_0, was a regular pentagon. The shape and global motion change of the configuration followed (11), (27) with $\Sigma_c = 0.0025 I_6$, $\sigma_s^2 = 0.0001$, $\sigma_\theta^2 = 0.25$, $A_c = 0.6 I_6$, $\alpha_s = 0.9$, $\alpha_\theta = 0.9$. The observations followed (29) with $\sigma_o^2 = 0.04$ and $p = 0.2$. I_6 denotes a 6×6 identity matrix. It is to be noted that the state transition prior (STP) of scale (e^{s_t}) is a log-normal and hence even $\sigma_s^2 = 0.0001$ results in a fairly broad distribution.

Whenever one or more landmarks are generated by clutter, the observation likelihood (OL) of log-scale (s_t) is either heavy-tailed with the wrong (outlier) mode or is multimodal. When many landmarks are generated by clutter, the same happens for θ_t. This combined with a broad prior of s_t, θ_t, results in multimodal $p^*(s_t, \theta_t)$. Whenever this happens, most particles of PF-Doucet end up sampling from a Gaussian about the wrong mode of $p^*(s_t, \theta_t)$ or of $p^*(s_t)$, resulting in loss of track. But PF-EIS does not suffer from this problem since it samples from the prior of s_t, θ_t. Also, since the prior of c_t is narrow compared to the distance between likelihood modes, $p^{**,i}(c_t)$ is usually unimodal and thus sampling from its Laplace approximation is valid. On the other hand, for small N_{pf}, PF-Gordon often loses track because it samples all states from the prior, thus resulting in small effective particle size. In Fig. 4(a), the mean squared error (MSE) plot averaged over 80 Monte Carlo runs is shown. Fig. 4(b) and Fig. 4(c) show examples where PF-Doucet and PF-Gordon lose track but PF-EIS does not. Also see Fig. 5 for MOCAP data, where PF-EIS with $N_{pf} = 50$

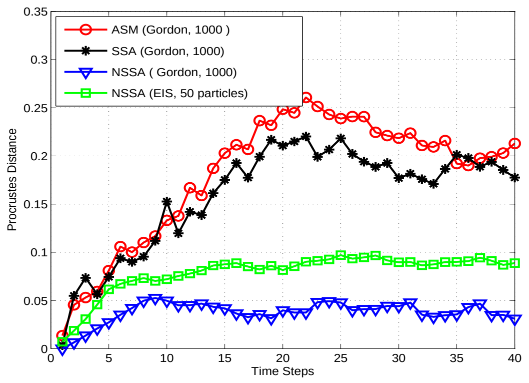

Fig. 5. Filtering noise and clutter corrupted MOCAP data: comparing NSSA, SSA and ASM based PF-Gordon and also NSSA based PF-EIS. NSSA significantly outperforms SSA and ASM. NSSA-based PF-EIS with just 50 particles has comparable performance to that of 1000 particle NSSA-based PF-Gordon (discussed in Sec. 5.3).

particles is able to achieve almost the same tracking accuracy as PF-Gordon with $N_{pf} = 1000$ particles.

5.3 Filtering from Noisy and Cluttered Observations

In this experiment, 2D landmark shape sequences from CMU Mocap database (refer Sec. 5.1) were used as the ground truth (shown in Fig. 6, top row). We incorporated random scale variations, additive noise and clutter to the ground truth. The observations were simulated using (29). This experiment helped us to quantitatively compare performance since ground truth was available.

We used the PF-Gordon (i.e. the basic PF) with $N_{pf} = 1000$ particles for filtering. Our primary objective was to compare the performance of NSSA based system model with that of SSA and ASM. PF-Gordon solely depends on the state transition prior (STP) for importance sampling and thus its performance heavily relies on the accuracy of the system model. Also, all past work on SSA or ASM based tracking used PF-Gordon.

We considered two motion activities namely *run* and *jump* with $K = 16$ landmarks. Different data sequences

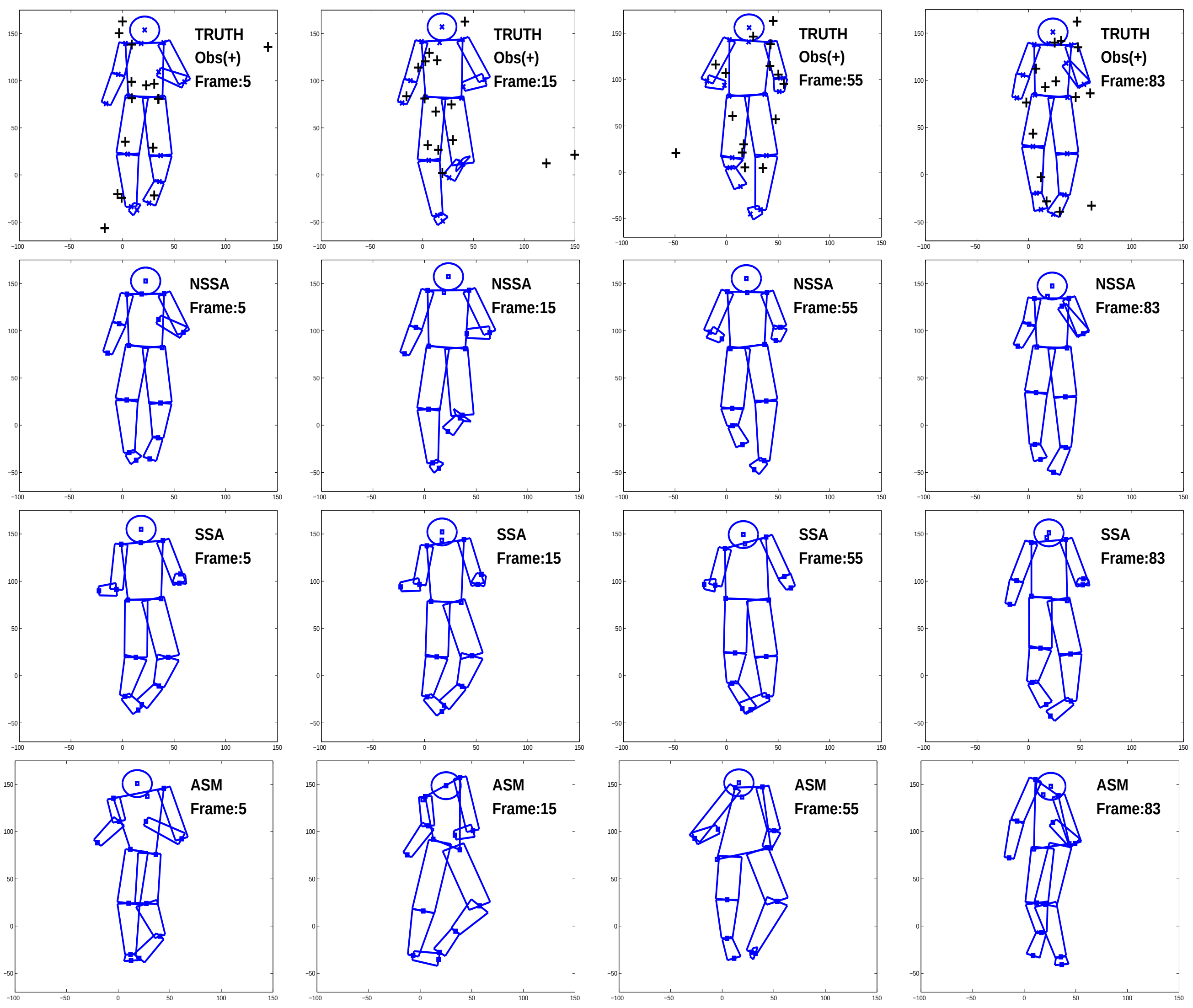

Fig. 6. Filtering out true shape data from noisy/cluttered observations using PF-Gordon (motion activity : *run*). The landmark points (denoted by $\times$ for ground truth and $\square$ for the filter output) are fitted with rectangular patches to visualize the body posture at a given time instant. The tracking performances of NSSA, SSA and ASM are shown over 4 frames. Top row: Ground truth with observations (**+**), second row: tracked with NSSA, third row: tracked with SSA and fourth row: tracked with ASM. It can be clearly seen that NSSA way outperforms SSA and ASM.

were used for training and testing. Our results are shown in Fig. 6 (run) and Fig. 7 (jump) and the procrustes distance comparison plots are given in Fig. 5. The landmark locations were fitted with rectangular patches to visualize the body posture at a given instant. The first row shows the ground truth and also the observation. It can be seen that the observed landmark locations (represented as **+** on top of the ground truth) were severely corrupted with clutter and random noise. Thus, visually, the observed configurations hardly conform to the human body. But, as shown in the second row of Fig. 6, NSSA has been able to filter out the true shape from those observations with very good accuracy. SSA (third row) and ASM (fourth row), however, perform poorly in this job. Similar results were found for motion activity *jump* (see Fig. 7). In Fig. 5, we plot the procrustes distance between the estimated shape and the true shape at each instant as the quantitative measure of filtering accuracy. Also note that PF-EIS (with NSSA model) is able to achieve almost the same accuracy as PF-Gordon (with NSSA model) with as few as $N_{pf} = 50$ particles.

In case of SSA and ASM, filtering performed around the fixed mean shape ends up generating shape samples far away from the desired shape space where the original set of deforming shapes lie. This, in turn, led to their poor performances. But NSSA, on the other hand, does an excellent job in filtering because of its time varying mean shape assumption. Of course, we assume that the shape deviations over successive time frames are small enough to make sure the the current shape is in

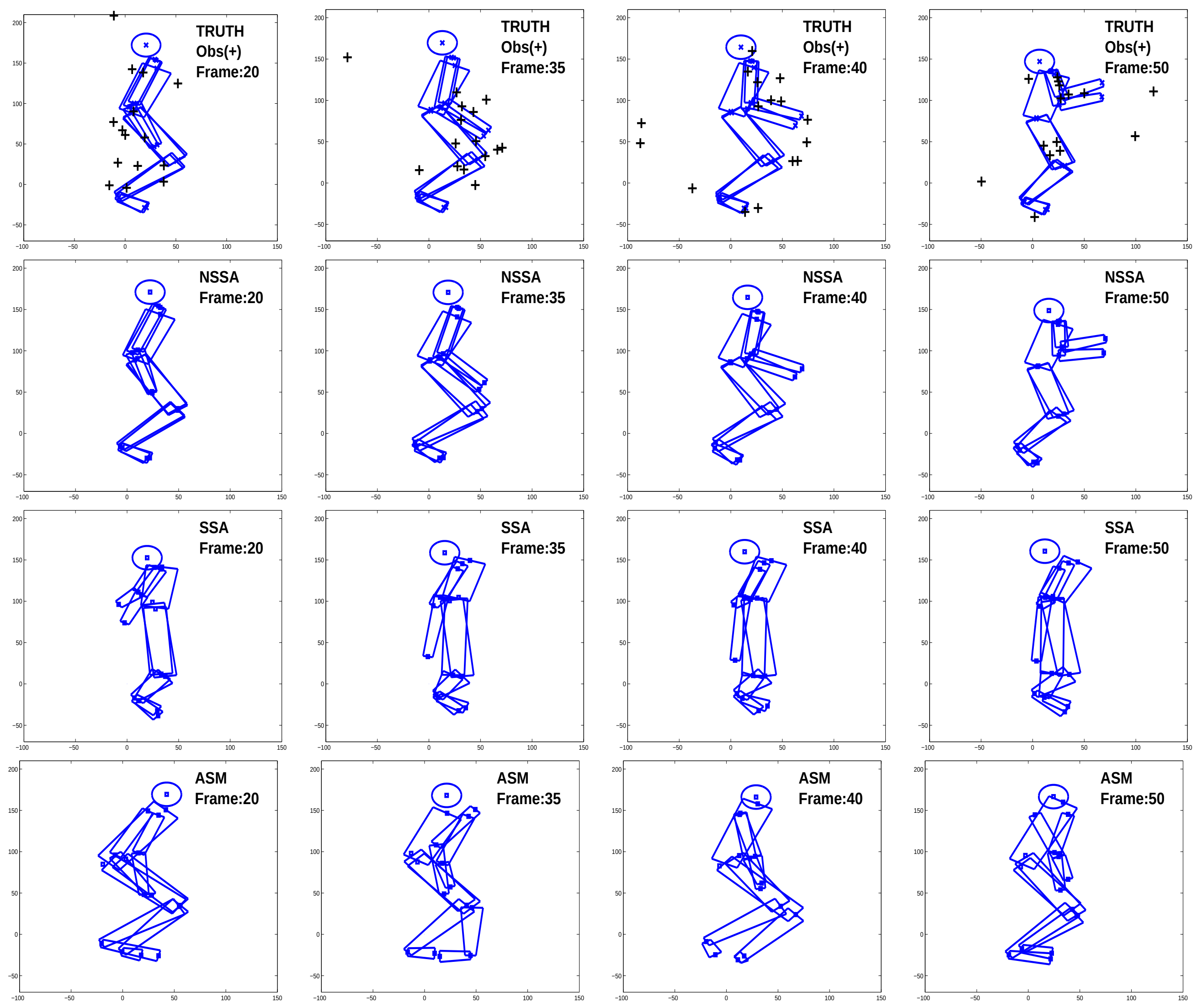

Fig. 7. Filtering out true shape data from noisy/cluttered observations using PF-Gordon (motion activity : *jump*). The landmark points (denoted by $\times$ for ground truth and $\square$ for the filter output) are fitted with rectangular patches to visualize the body posture at a given time instant. The tracking performances of NSSA, SSA and ASM are shown over 4 frames. Top row: Ground truth with observations (**+**), second row: tracked with NSSA, third row: tracked with SSA and fourth row: tracked with ASM. It can be clearly seen that NSSA way outperforms SSA and ASM

the neighborhood of the current mean shape (i.e. the previous shape) for our mathematical treatments to be valid. This is a reasonable assumption for most of the real-life motion activities.

5.4 Tracking and Automatic Landmark Extraction

For automatic landmark extraction and tracking, we used 50 frames of real-life videos of human activities (shown in Fig. 8 (run) and Fig. 9 (jump)). A total of 13 body landmarks were considered as shown in Fig. 9. The chosen body landmarks were: right shoulder, right elbow, right hand, right hip, right knee, right foot, head, left shoulder, left elbow, left hand, left hip, left knee, left foot.

For run sequences, the system model was learnt from the hand-marked ground truth data corresponding to the training database. In case of jump, however, we used the mocap data itself. We appropriately subsampled the mocap data frames in order to roughly synchronize them to the video frames. Implementations of Algorithm. 4 using system models based on based on NSSA, SSA and ASM were compared. Their performances over multiple time frames are shown in Fig. 8 (run). It can be clearly seen that NSSA (top row) performs much better than SSA (second row) or ASM (third row) in terms of *keeping track* of the body landmarks. It is very important to note that filtering and prediction play a very crucial role in the process of extracting landmark observations. To verify this, we extracted the landmark observations purely based on optical flow i.e. starting with the initial locations we used the optical flow between successive

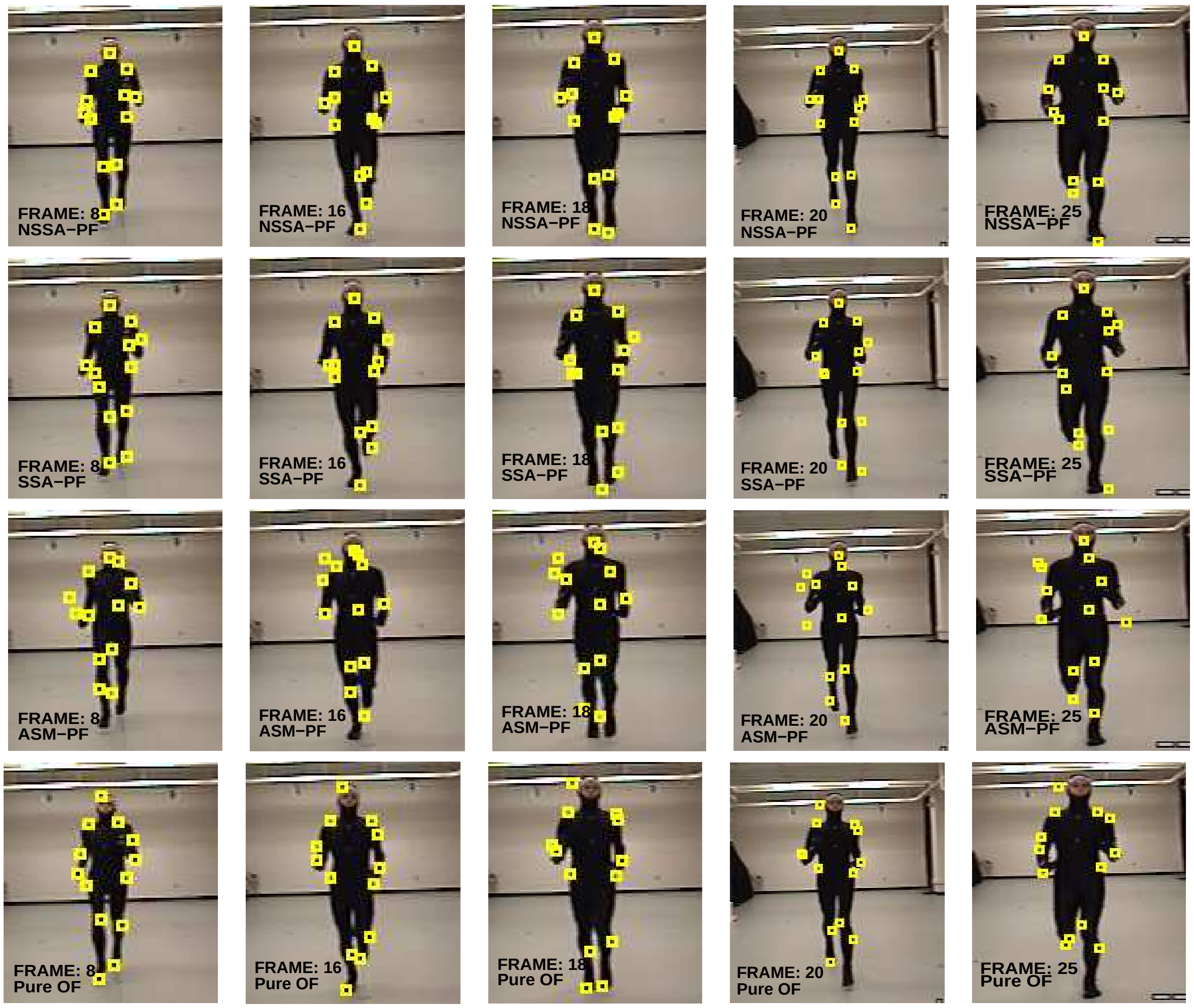

Fig. 8. Tracking landmark configurations over the video of a running sequence (discussed in Sec. 4.5). Top row: NSSA, second row: SSA and third row: ASM. It can be clearly seen that NSSA way outperforms SSA and ASM. Fourth row: landmark observations extracted using purely optical flow based approach. It can be seen that the observed landmark loses posture information gradually over time. Such observation lead to poor filtering/tracking performance of the system.

frames to drift the points and thus getting observations over time. This procedure does not use the knowledge of the state estimates at each instant to decide where the expected landmark might be while computing the optical flow. As can be seen from Fig. 8 (fourth row), quite a few of the observed landmarks in this case were found to get stuck at wrong locations (due to background interference, occlusion or clutter) and from that point on they were never in sync with the body movements. In fact, the point of using the state estimates is to correct the locations of such landmarks and making sure that we do not end up computing the OF at the wrong regions for getting the landmark location for the next frame.

Next, we test the system with NSSA based system model on the video of a person *jumping*. It can be seen in Fig. 9 that NSSA did a very good job in terms of tracking the landmarks over various time frames. It is to be noticed that at frame 15, it loses track of the landmark corresponding to the right hand. But later, it regains the track (see frame 39, Fig. 9).

5.5 3D-NSSA Synthesis

Motivated by the drastically small modeling error of 3D-NSSA for human actions (see Fig. 3(b)), we attempted to use 3D NSSA for a motion synthesis application. We learnt the deformation model for 3D body shape of the human body while running from MOCAP data. The synthesized run sequence using this model is shown in Fig. 10. Since there is no ground truth is this case, we

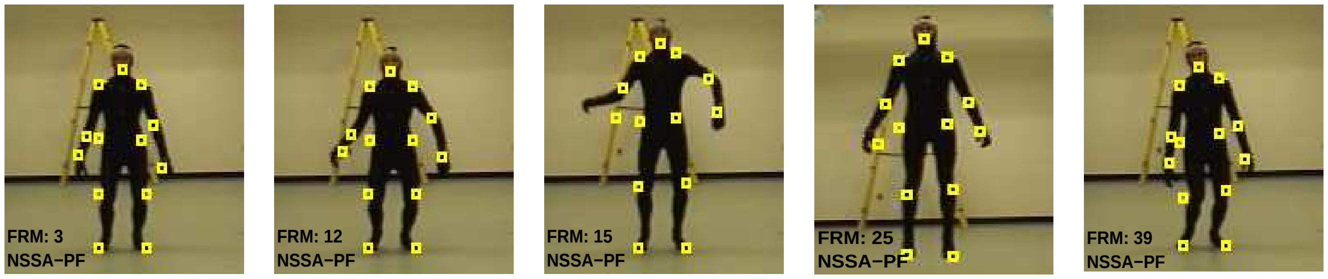

(a) Frame 3 (b) Frame 12 (c) Frame 15 (d) Frame 25 (e) Frame 39

Fig. 9. Tracking landmark configurations over the video of a jump sequence with NSSA based system model (discussed in Sec. 4.5). It can be seen that at frame 15, NSSA lost track of one of the landmarks (right elbow). But after that it regains track of the landmark.

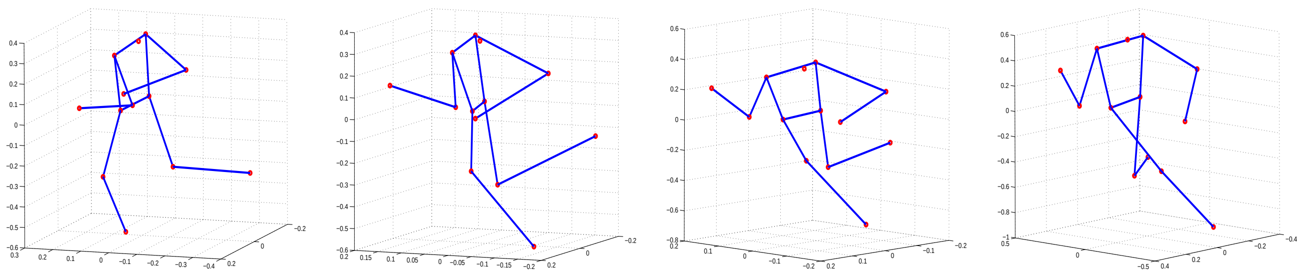

(a) Frame 10 (b) Frame 45 (c) Frame 51 (d) Frame 72

Fig. 10. Synthesis of a 3D shape sequence corresponding to motion activity *run*. Four frames are shown. The system model was learnt using 3D-NSSA on 3D landmark shape sequences for running. The sequence shown above visually resembles a running sequence.

visually verified the systems ability to synthesize *run* and the system performance was found to be promising.

5.6 Change Detection with NSSA

We did a simple experiment to test the ability of the NSSA-based tracker to detect changes in activity while still not completely losing track. We used a sequence where a person begins by running and then leaps (http://mocap.cs.cmu.edu:8080/subjects/49/49_04.avi). Notice that this is a fairly sudden change. The ELL-based change detection statistic [38] was able to detect the change to leap, and for sometime after the change also, our tracker did not lose track (see Fig. 11 - tracking error does not increase until later). More results and comparison with SSA are shown in [1] (due to lack of space, we do not put them here).

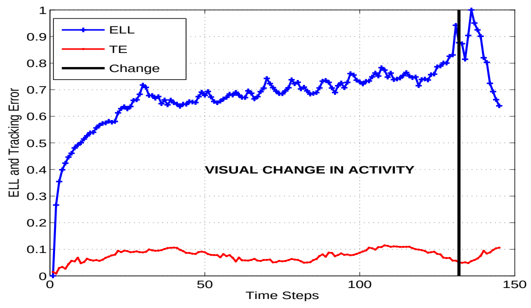

Fig. 11. The ELL and tracking error (TE) plot for the shape sequence with *run* followed by *leap*. PF-Gordon was used with NSSA based system model. The actual activity transition occurred at $t = 132$. It can be clearly seen that ELL detected the change. There is distinct spike of ELL around $t = 132$. However, the tracker still keeps tracking even after the change has occurred.

6 Conclusions and Future Work

The key contribution of this work is a novel approach to define a generative model for both 2D and 3D nonstationary landmark shape sequences, which we call nonstationary shape activity (NSSA). The main idea is to compute the tangent space representation of the current shape in the tangent space at the previous shape. This can be referred to as the shape velocity vector since it quantifies the difference between two consecutive shapes projected into the tangent space at the first one. The "aligned" shape velocity coefficients (shape speed vector) are modeled using standard vector time series methods.

Applications in filtering, tracking, synthesis (using 3D-

NSSA models) and change detection are demonstrated. Filtering and tracking are studied in detail and significantly improved performance over related work is demonstrated (see Figs. 4-10). With the exception of smoothing splines [13], [21], most other existing work does not model nonstationary shape sequences. Smoothing splines is not a generative model and hence is not applicable for tracking, Bayesian filtering or synthesis. In other work [7] we have also successfully demonstrated the use of the NSSA for model-based compression of landmark shape sequence data.

Future work includes evaluating the recognition and change detection application in more detail. As explained earlier, piecewise ASMs or SSAs are good for recognition problems, but not for automatic tracking, since they do not model the transitions between pieces well. For automatic landmark extraction from image sequences followed by recognition, one could use an NSSA based tracker to extract the landmark sequences, followed by a piecewise ASM or SSA based recognizer as in past work. For change (or abnormality) detection, as demonstrated in Fig. 11 and also in [1], NSSA can again be successfully used.

Another possible future work is combining our models with GPVLMs based observation extraction techniques [16], [30]. Also, our optical flow based landmark extractor could be improved by using ideas from [39].

References

[1] N. Vaswani and R. Chellappa, "Nonstationary shape activities," in *IEEE Conf. Decision and Control (CDC)*, December 2005.

[2] N. Vaswani and S. Das, "Particle filter with efficient importance sampling and mode tracking (pf-eis-mt) and its application to landmark shape tracking," in *Asilomar Conference on Signals, Systems and Computers*, 2007.

[3] D. Kendall, D. Barden, T. Carne, and H. Le, *Shape and Shape Theory*. John Wiley and Sons, 1999.

[4] N. Vaswani, A. RoyChowdhury, and R. Chellappa, ""Shape Activity": A Continuous State HMM for Moving/Deforming Shapes with Application to Abnormal Activity Detection," *IEEE Trans. Image Proc.*, pp. 1603–1616, October 2005.

[5] R. Hartley and A. Zisserman, *Multiple View Geometry in Computer Vision*. Cambridge University Press, 2000.

[6] "CMU Motion Capture Data," *Available at: http://mocap.cs.cmu.edu/*.

[7] N. Vaswani, "Kalman filtered compressed sensing," in *IEEE Intl. Conf. Image Proc. (ICIP)*, 2008, submitted.

[8] A. Veeraraghavan, A. RoyChowdhury, and R. Chellappa, "Matching shape sequences in video with an application to human movement analysis," *IEEE Trans. Pattern Anal. Machine Intell.*, vol. 27, no. 12, pp. 1896–1909, 2005.

[9] I. Dryden and K. Mardia, *Statistical Shape Analysis*. John Wiley and Sons, 1998.

[10] T. Cootes, C. Taylor, D. Cooper, and J. Graham, "Active shape models: Their training and application," *Computer Vision and Image Understanding*, vol. 61, pp. 38–59, January 1995.

[11] M. Isard and A. Blake, "Condensation: Conditional Density Propagation for Visual Tracking," *Intl. Journal Comp. Vis.*, pp. 5–28, 1998.

[12] N. J. Gordon, D. J. Salmond, and A. F. M. Smith, "Novel approach to nonlinear/nongaussian bayesian state estimation," *IEE Proceedings-F (Radar and Signal Processing)*, pp. 140(2):107–113, 1993.

[13] A. Kume, I. Dryden, H. L. Le, and A. Wood, "Fitting cubic splines to data in shape spaces of planar configurations," in *Leeds Annual Statistics Research*, 2002.

[14] T.F.Cootes, G. Edwards, and C.J.Taylor, "Active appearance models," in *European Conf. on Computer Vision*, vol. 2, pp. 484–498, 1998.

[15] B. P. Lelieveldt, R. J. van der Geest, J. H. C. Reiber, J. G. Bosch, S. C. Mitchel, and M. Sonka, "Time-continuous segmentation of cardiac image sequences using active appearance motion models," *IPMI*, pp. 446–452, January 2001.

[16] T. Tai-Peng, L. Rui, and S. Sclaroff, "Tracking human body on a learned smooth space," in *Boston University Computer Science Tech. Report No. 2005-029*, 2005.

[17] S. Hou, A. Gatala, F. Caillette, N. Thacker, and P. Bromiley, "Real-time body tracking using a gaussian process latent variable model," in *IEEE Intl. Conf. on Computer Vision (ICCV)*, October 2007.

[18] T. Cootes, C. Taylor, D. Cooper, and J. Graham, "Training Models of Shape from Sets of Examples," in *British Machine Vision Conference*, pp. 9–18, 1992.

[19] N. Paragios, M. Jolly, M. Taron, and R. Ramaraj, "Active shape models and segmentation of the left ventricle in echocardiography," in *5th Intl. Conf. on Scale Space and PDE Methods in Computer Vision, Hofgeismar, Germany*, April 2005.

[20] B. Song, N. Vaswani, and A. K. Roy-Chowdhury, "Closedloop tracking and change detection in multi-activity sequences," in *IEEE Conf. on Computer Vision and Pattern Recognition (CVPR)*, 2007.

[21] A. Kume, I. Dryden, and H. Le, "Shape space smoothing splines for planar landmark data," *Biometrika*, 2007, to appear.

[22] A. Srivastava, "Prior models for bayesian filtering in subspace tracking," in *First IEEE Sensor Array and Multichannel Signal Processing Workshop*, 2000.

[23] C. Zahn and R. Roskies, "Fourier descriptors for plane closed curves," *IEEE Trans. on Computers*, vol. C-21, pp. 269–281, 1972.

[24] M. Isard and A. Blake, "Contour tracking by stochastic propagation of conditional density," *Eur. Conf. on Comp. Vis. (ECCV)*, pp. 343–356, 1996.

[25] A. Srivastava, W. Mio, E. Klassen, and S. Joshi, "Geometric analysis of continuous planar shapes."

[26] J. A. Sethian, *Level Set Methods and Fast Marching Methods*. Cambridge University Press, 2nd ed., 1999.

[27] S. X. Ju., M. J. Black, and Y. Yacoob, "Cardboard people: A parameterized model of articulated image motion," in *Proceedings of the 2nd International Conference on Automatic Face and Gesture Recognition*, 1996.

[28] R. Ishiyama, H. Ikeda, and S. Sakamoto, "A compact model of human postures extracting common motion from indivisual samples," in *Intl. Conf. on Pattern Recognition*, 2006.

[29] A. Aggrawal. and B. Triggs, "Tracking articulated motion with piecewise learned dynamical models," in *European Conf. on Computer Vision*, 2004.

[30] N. Lawrence, "Probabilistic non-linear principal component analysis with gaussian process latent variable models," *Journal of Machine Learning Research*, pp. 1783–1816, November 2005.

[31] J. Shi and C. Tomasi, "Good features to track," in *IEEE Conf. on Comp. Vis. Pat. Rec. (CVPR)*, pp. 593–600, 1994.

[32] A. Doucet, "On sequential monte carlo sampling methods for bayesian filtering," in *Technical Report CUED/F-INFENG/TR. 310, Cambridge University Department of Engineering*, 1998.

[33] L. Tierney and J. B. Kadane, "Accurate approximations for posterior moments and marginal densities," *J. Amer. Stat. Assoc*, vol. 81 (393), pp. 82–86, March 1986.

[34] S. Arulampalam, S. Maskell, N. Gordon, and T. Clapp, "A tutorial on particle filters for on-line non-linear/non-gaussian bayesian tracking," *IEEE Trans. Sig. Proc.*, vol. 50, pp. 174–188, Feb. 2002.

[35] V. Cevher and J. H. McClellan, "Proposal strategies for joint state-space tracking with particle filters," in *IEEE Intl. Conf. Acoustics, Speech, Sig. Proc. (ICASSP)*, 2005.

[36] N. Vaswani, "Particle filtering for large dimensional state spaces with multimodal observation likelihoods," *IEEE Trans. Sig. Proc.*, October 2008.

[37] S. Khan, "Matlab code for optical flow using lucas kanade method," *www.cs.ucf.edu/ khan/*.

[38] N. Vaswani, "Additive change detection in nonlinear systems with unknown change parameters," *IEEE Trans. Sig. Proc.*, pp. 859–872, March 2007.

[39] A. Srivastava and H. Jermyn, "Looking for shapes in two-dimensional cluttered point clouds," *IEEE Trans. Pattern Anal. Machine Intell.*, to appear.